

Apprenticeship at the IBM Almaden Research Center

A. V. Joura

Department of Physics, Georgetown University, DC

April 17, 2006

Abstract

From June 2004 to May 2005, as part of the requirement of our Ph.D. program, I worked as an apprentice under the supervision of Barbara Jones at the IBM Almaden Research Center.

1 IBM

During its almost a century history IBM was mainly known as a leader in a “tabulator” business. Starting with tabulators in 1911 (that time they were sold by a company called CTR, T. J. Watson changed its name to IBM in February of 1924), followed by calculator (aka large-scale automatic digital computer) Mark-1, then big mainframe computers and finally personal computers, IBM has stayed a leader in this new computer business. IBM was also a leader in many computer-related areas like storage devices, servers, databases, and this was mainly achieved by acquisitions in software products.

IBM has undergone pretty dramatic changes starting in December 2002, when they sold their disk drive business to Hitachi. This was followed by a sale of their PC business to Lenovo in December 2004. Right now, IBM still has some parts of what is considered its traditional business, namely they didn’t abandon their server business, they are making special purpose chips and even have opened a 300 mm chip-making plant in July 2002 in New York state. It probably can also be said that one of IBM’s biggest high tech businesses – the database division – is in good health. But based on what has happened to IBM since they adopted a corporate strategy to enter the service sector and leave the commodity businesses (hard drive and PC businesses nowadays are, in fact, very low-profit-margin businesses), it probably can be concluded that people who knew what IBM was in 20th century will find it difficult to recognize its new face in 21st century. As the on-line newspaper InfoWorld says, “Since 2002, IBM has spent about \$9 billion to acquire over 30 companies including Price Waterhouse Coopers Consulting. In the same period, it has divested several businesses where it lacks scale or market opportunities, such as its hard-disk drives and displays units.”[1] So it’s likely that in ten years we may find IBM being a large investment bank or a consulting firm.

2 IBM Almaden Research Center

The Almaden research center, one of IBM’s world-renowned research facilities, was hurt considerably by the changes IBM has undergone in recent years. In particular, the IBM Almaden center’s Science and Technology division, which is involved in basic and applied research in condensed matter physics, was hurt the most. A large part of the division, involved in hard disk drive research, was sold to Hitachi and currently Hitachi and IBM are sharing the same building. There are still IBM Almaden groups involved in novel magnetic/non magnetic storage technology research. Stuart Parkin’s (IBM Fellow) group, for example, has recently developed a working prototype of a non-volatile MRAM memory chip based on Magnetic Tunnel Junctions (MTJs). Dan Rugar’s group was involved in the development of a so called Millipede high-density storage device based on the principle of Atomic Force Microscopy (AFM), and right before the sale of the hard disk drive business to Hitachi, Kumar Wickramasinghe (IBM Fellow) was developing a novel technology for increasing the storage density of usual hard drives by heating “bits” of magnetic medium before writing to them. But after IBM got rid of its magnetic storage technology, a necessary and important link between research and development

was lost and this, in my opinion, adversely affected the motivation of research as well as the spirit of Almaden employees in the Science and Technology division. This link is important because working with IBM product developers to use knowledge gained by researchers in creating new products and in improving existing IBM products is what distinguishes an industrial lab from an academic one and justifies its existence.

3 Research

My research at Almaden consisted of four parts, two of which were not related directly to work done at Almaden, and two that were. The latter ones were theoretical investigations of the so-called mirage effect and of domain wall motion in magnetic wires. These topics are described in detail below.

3.1 Different energies in magnetic materials: Theoretical background

We will consider the energies of magnetic metals. A magnetic metal typically has both conduction and localized electrons. We assume that such a metal can be described using a “classical” picture of magnetism, namely, that the magnetization \mathbf{M} is created by localized electrons and to a good approximation its magnitude can be considered to be constant: $|\mathbf{M}| = \text{const}$. In the absence of current, the wire has an equilibrium distribution of the magnetization $\mathbf{M}(\mathbf{r})$. This equilibrium distribution is determined by the minimization of a free energy functional $F[\mathbf{M}(\mathbf{r})]$ which includes the following terms (for details see [2]):

1. Exchange energy E_{ex}

This is the energy required by a nonuniform magnetization \mathbf{M}^1 :

$$E_{ex} = \frac{1}{2} \int \alpha_{ik} \frac{\partial M_l}{\partial x_i} \frac{\partial M_l}{\partial x_k} d^3 \mathbf{x} \quad (1)$$

where α_{ik} is a material specific symmetric tensor.

2. Anisotropy energy

This energy reflects the fact that different directions of magnetization have different energies because of spin-orbit and spin-spin interactions of electrons with the crystal nuclei (whose positions are fixed at the lattice sites) and has the form

$$E_{an} = \int \frac{K_{ik}}{|\mathbf{M}|^2} M_i M_k d^3 \mathbf{x} \quad (2)$$

where K_{ik} is a material specific symmetric tensor.

3. Magnetoelastic energy

This energy arises due to a deformation of the crystal; it has both a relativistic and exchange component, and is written as

$$E_{me} = \int \frac{1}{|\mathbf{M}|^2} a_{iklm} \tilde{\sigma}_{lm} M_i M_k d^3 \mathbf{x} \quad (3)$$

where a_{iklm} is a material specific tensor that is symmetric in ik and lm and $\tilde{\sigma}_{lm}$ is the elastic strain tensor.

4. Magnetostatic energy.

This energy is the energy of the magnetic field itself. The density of the magnetostatic energy is expressed as

$$E_{ms} = -\mathbf{M} \cdot \mathbf{H} - \frac{H^2}{8\pi} . \quad (4)$$

¹We assume a summation over repeated indices.

The magnetic field created by a static distribution of magnetization can be described using an electrostatic analogy. This means that to find the magnetic field strength \mathbf{H} , we need to find a field created by “magnetic” charges with volume density $\rho_m = -\text{div}\mathbf{M}$ and surface density $\sigma_m = M_n$, where M_n is the normal component of the magnetization on the surface of the magnetic material². So, the equation and the boundary condition for \mathbf{H} read

$$\begin{aligned}\text{div}\mathbf{H} &= 4\pi\rho_m \\ H_n &= -4\pi\sigma_m\end{aligned}\tag{5}$$

which are, as was already said, completely equivalent to the equations obeyed by a static electric field. This approach allows us to rewrite the magnetostatic energy as

$$E_{ms} = \frac{1}{2} \int_V \varphi \rho_m dV\tag{6}$$

and interpret this energy as the energy of “magnetic charges” in a magnetic field with the potential

$$\varphi(\mathbf{r}) = \int_V \frac{\rho_m(\mathbf{r}')}{|\mathbf{r} - \mathbf{r}'|} d^3\mathbf{r}' ,\tag{7}$$

where ρ_m is assumed to incorporate the surface charges σ_m through δ -functions³.

3.2 Domain wall motion in magnetic nano-wires: Experiment

My theoretical work on domain wall motion was motivated by an article by G.Tatara et al. [4] which explored the notion of current-induced domain wall motion. Let’s describe the physics of this phenomenon.

Magnetic wires, which are of interest for us, have two particular features. First, they are created by some deposition process (like sputtering, electron beam or molecular beam deposition). That means that deformations are virtually absent and the magnetoelastic energy can be disregarded.⁴ Second, the cross section of the wires is very small (in the experiment in [5] the wires used had a cross section of $70 \times 45 \text{ nm}$). Because of this small size, it is energetically unfavorable to have an inhomogeneity within the cross sectional plane, because this would create too large of an exchange energy. So, it is energetically favorable to have a uniform magnetization distribution along the length of the wire. The orientation of the magnetization along the largest length reduces the value of magnetostatic energy created by the “magnetic” charges on the exterior surface of this rectangular-shaped wire. Once we realize that the equilibrium distribution of the magnetization is uniform and points along the wire (two possible directions) it is easy to see that the only possible domain structure for such a wire is the so-called “head-to-head” domain (see Figure 1). This is when the magnetization in neighboring domains points in opposite directions.

Let’s briefly describe the experimental setup which was used to study domain wall motion (details can be found in [5]) and then proceed to our theoretical investigations. In the experiment, such a wire with two head-to-head domains was bent and put into an external magnetic field (see Figure 2).

When the magnetic wire is placed in a sufficiently weak magnetic field \mathbf{H} , this field doesn’t change the distribution of the magnetization in the wire. Then we only need to account for an additional magnetostatic energy (6), where ρ_m is the density of the surface magnetic charges on the sides of the wire, where magnetization has a non-zero normal component and $\varphi(\mathbf{r})$ is the potential created by the magnetic field \mathbf{H} : $\varphi(\mathbf{r}) = \mathbf{H} \cdot \mathbf{r}$. It is easy to see that, when the wall moves, this energy changes in the same way as the potential energy of a pendulum in a uniform gravitational field.

To move the wall from equilibrium position, a spin polarized current was used. A detailed description of the physics behind that effect would take more space than we can afford to allocate in this short report, so we are referring the reader to the article by Tatara et al. [6] and the references therein.

²Here we assume that the component M_n is calculated with respect to the magnetic material’s outwardly pointing normal vector.

³For a more detailed description of the electrostatic analogy see [3].

⁴For the magnetoelastic energy to play a role tensions are usually introduced using fast cooling from a melt.

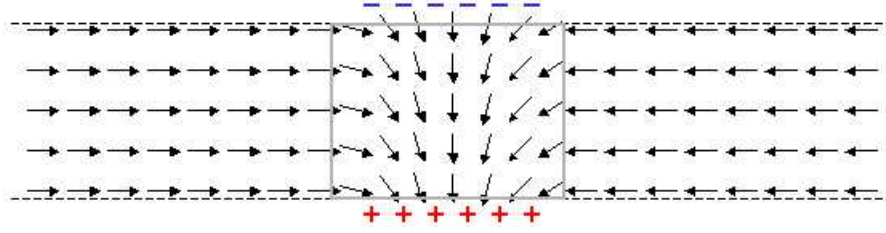


Figure 1: Model distribution of magnetization in a head-to-head domain structure. In such a structure, the magnetization to the left and to the right points in opposite directions along the wire; a particular distribution of the magnetization inside the domain wall (the gray box) is determined by minimizing the thermodynamic potential. In our case, it is a competition between the magnetostatic and exchange energies. “+” and “-” signs denote magnetic charges created on the sides of the wire, where the magnetization has a non-zero normal to the wire surface component.

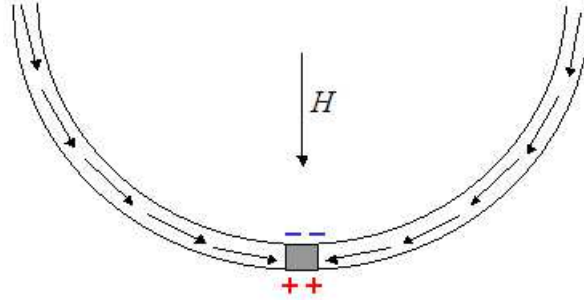


Figure 2: A head-to-head domain wall in a weak magnetic field H can be regarded as a magnetic dipole, which can move along the wire. Its energy is then essentially the energy of a pendulum in a uniform gravitational field.

3.3 Domain wall motion in magnetic nano-wires: Theory

A detailed theory of the motion of magnetic domain walls can be found elsewhere (see [4] and references therein, for example). The wall can be described by two parameters, an angle Ψ and a coordinate of the wall q . The angle Ψ is the polar angle of the magnetization in the spherical system of coordinates. These two parameters satisfy a system of differential equations

$$\dot{q} = -\alpha(\omega_{pin}q - \beta u) + u_c \sin 2\Psi + u \quad (8)$$

$$\dot{\Psi} = -\frac{1}{\Delta}(\omega_{pin}q - \beta u) - \frac{\alpha}{\Delta}(u_c \sin 2\Psi + u) \quad (9)$$

where we have the following parameters: Δ is the domain wall width, α is the Gilbert damping, which reflects the rate of energy loss when the magnetization vector is moving; a is the length of the unit cell, and S is the spin per unit cell (from which the magnitude of the magnetization of the material can be found: $M_s = 2S\mu_B/a^3$). The parameter u_c ,

$$u_c = \frac{\Delta SK_{\perp}}{2\hbar} , \quad (10)$$

is proportional to the anisotropy field K_{\perp} of the wire⁵. The parameter u

$$u = v_{el} = \frac{a^3}{2eS} j_s \quad , \quad (13)$$

characterizes the so-called spin transfer, where j_s is the density of the spin current. This spin transfer arises because of a directional mismatch between the wall magnetization and the spin polarization of the current. As conduction electrons travel through the wall a torque is exerted by the wall on the electrons, which tries to align the electrons spin directions with the magnetization direction of the wall. This means that a torque of the same magnitude is exerted on the wall by the electrons.

The spin torque is not the only “force” acting on the wall. The other interaction, called momentum transfer, is independent of the spin direction, and arises because of the reflection of electrons from the wall, which (reflection) is proportional to the wall’s resistance:

$$F_{el} = enR_{DW}IA \quad (14)$$

where A is the cross sectional area of the wire, I is the current through the wire, R_{DW} is the domain wall electrical resistance, and n is conduction electron density. In equations (8,9), the momentum transfer strengt is included in the term β , which is proportional to the ratio F_{el}/v_{el} :

$$\beta = \frac{a^3 \Delta}{2\hbar AS} \cdot \frac{F_{el}}{v_{el}} \quad (15)$$

The remaining parameter is ω_{pin} , which reflects the strength of the pinning potential. The pinning potential, that enters the Hamiltonian of the system, is a parabolic potential

$$V_{pin} = AVq^2 \quad (16)$$

where V characterizes the strength of the potential. In fact, it can be any potential depending on the wall position q . For example, defects in the wire create potential barriers or, maybe, potential traps. In our case, the potential energy arises as a consequence of the interaction of the wall’s magnetic dipole⁶ with the external magnetic field which, for small deviations of the wall from the equilibrium position $q = 0$, is quadratic in q . Then the pinning frequency ω_{pin} is defined as

$$\omega_{pin} = \gamma \frac{\Delta V}{M_s} \quad . \quad (17)$$

Another natural frequency, which arises from equations (8,9), is ω_K

$$\omega_K = \frac{u_c}{\Delta} \quad , \quad (18)$$

which is the inverse time for an object moving with velocity u_c to cross the length Δ of the domain wall.

Equations (8,9) can be significantly simplified, if we rewrite them using the following dimensionless variables [7]:

$$x = \frac{q}{\Delta} \quad , \quad \tau = \omega_K t \quad , \quad v = \frac{u}{u_c} \quad , \quad r = \frac{\omega_{pin}}{\omega_K} \quad . \quad (19)$$

Then equations (8,9) become

⁵Note, although, that it’s not a usual anisotropy field due to crystalline structure of the material, which – in the experiment considered – is amorphous, not crystalline; it is the field, characterizing the asymmetry of the wire in xy -plane due to demagnetizing fields:

$$U_{df} = K_1 m_x^2 + K_2 m_y^2 + K_3 m_z^2 = \sin^2 \theta (K_1 \cos^2 \phi + K_2 \sin^2 \phi - K_3) + K_3 = \sin^2 \theta (K_1 - K_3 + (K_2 - K_1) \sin^2 \phi) + K_3 \quad . \quad (11)$$

Dropping a constant term K_3 , we get

$$U_{df} = \sin^2 \theta (K + K_{\perp} \sin^2 \phi) \quad (12)$$

⁶See sections 3.1 and 3.2 for explanation of the meaning of magnetic charge and dipole.

$$\begin{aligned}\frac{\partial x}{\partial \tau} &= -\alpha(rx - \beta v) + (\sin 2\Psi + v) \\ \frac{\partial \Psi}{\partial \tau} &= -(rx - \beta v) - \alpha(\sin 2\Psi + v).\end{aligned}\quad (20)$$

There is an analogy of equations (20) with the so-called resistively shunted junction (RSJ) model for current flow in a Josephson junction. Consider a Josephson junction, connected in parallel with a capacitor C and a resistor R , driven by an (ac) current source I (see Fig. 3).

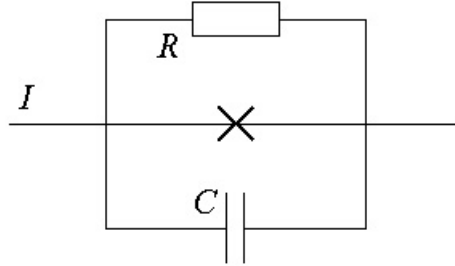


Figure 3: Equivalent circuit for the RSJ Josephson junction model.

Such a junction is also described by a pair of coupled differential equations:

$$\begin{aligned}C\dot{V} &= -\frac{V}{R} + I - I_c \sin \phi \\ \dot{\phi} &= \frac{2e}{\hbar}V\end{aligned}\quad (21)$$

where I_c is a characteristic current of the junction, V is a voltage drop through the junction, and ϕ is the quantum-mechanical phase difference between the two superconductors.

It was observed [7] that equations (21) look very similar to equations (20) for domain wall motion. This becomes obvious when we rewrite equations (21) in a dimensionless form using the parameters ($V_c = I_c R$, $\omega_c = 2eV_c/\hbar$, $\tau = RC$) $x = V/V_c$, $i = I/I_c$, and $r = \omega_c \tau = (2e/\hbar)I_c R^2 C$. Then equations (21) become

$$\begin{aligned}x'_\xi &= -x + i - \sin \phi \\ \phi'_\xi &= rx\end{aligned}\quad (22)$$

where time derivatives are taken with respect to dimensionless time $\xi = t/\tau$ (we see that in this form the only parameter, which defines a behavior of the junction, is the dimensionless parameter r).

We should stress that equations (20) and (22) are only “similar”: there is no set of parameters where these equations become equivalent (or at least not an obvious one). But we can hope that their similarity will give rise to similar behavior of their solutions. Indeed this turns out to be true.

The Josephson junction equations (22) display an unusual behavior called Shapiro steps. The essence of this effect can be described as follows. Let’s assume that first the driving current i is a constant $i = i_{dc}$ and we set up an experiment where we measure the average voltage drop \bar{x} versus the DC current magnitude i_{dc} . Figure 4 shows this dependence. For $i_{dc} > 1$, the average voltage \bar{x} exhibits a monotonic growth shown in the black curve in Fig. 4.

Interesting behavior is observed when we turn on an additional AC current⁷:

⁷The ac current for Josephson junctions is in the microwave frequency range, so “turning on” here means inducing it using so-called microwave transmission lines.

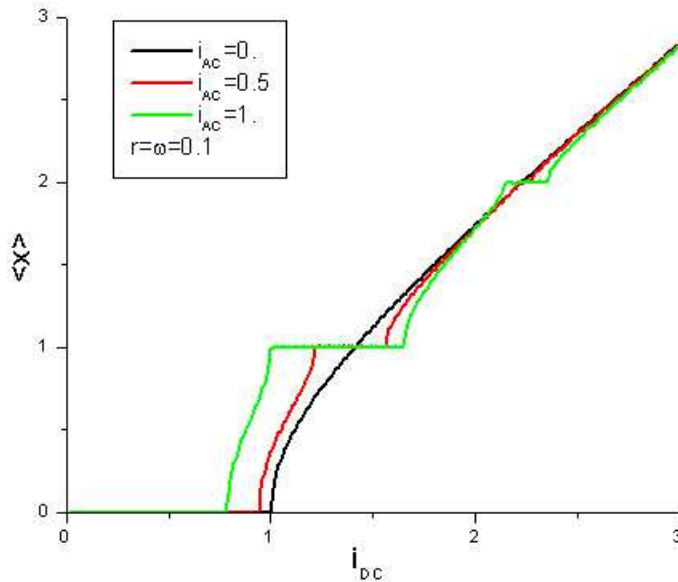


Figure 4: Average dimensionless voltage $\langle x \rangle$ as a function of dimensionless driving dc-current amplitude i_{dc} for several ac-current amplitudes, (a) $i_{ac} = 0$ – black curve (b) $i_{ac} = 0.5$ – red curve (c) $i_{ac} = 1$ – green curve.

$$i = i_{dc} + i_{ac} \sin(\omega_{ac} \xi) . \quad (23)$$

When the magnitude of the DC current i is close to $\omega_{ac} n / r$ (with n an integer), the average voltage \bar{x} stops to grow with increasing i_{dc} . This effect is called mode-locking or Shapiro steps⁸. Figure 4 illustrates this effect.

Our goal is to find out whether solutions of the system of equations (20) illustrate similar behavior to what is found in the equations describing a Josephson junction, namely Shapiro steps. We solved these equations using different sets of parameters α , β , r and v and found that indeed plots of the average displacement \bar{x} versus v_{dc} do show Shapiro-step behavior. It turns out that these plots show even more rich and interesting behavior, including hysteresis and Shapiro steps at fractional frequencies. The following pictures and descriptions briefly describe our findings.

Let’s first discuss the numerical values of the parameters we used. From [5] it can be found [7] that $\alpha \sim 10^{-2}$, $\beta \sim 1$ and $r \sim 10^{-4}$. The value of u is determined by the current through the wall. A natural scale for v is 1 because $v = 1$ is the value of current when Walker breakdown happens in the absence of pinning potential. We apply

$$v = v_{dc} + v_{ac} \sin(\omega_{ac} \tau) \quad (24)$$

The frequency of forced oscillations ω_{ac} is chosen in such a way that the first Shapiro step occurs at $v_{dc} \sim 1$.

First let’s consider the case when $v_{ac} = 0$. The ultimate technological goal of current-induced domain wall motion is to displace domain walls as far as possible by the smallest possible currents. A theoretical investigation of the system (20) showed [7] that there exists a so-called “attraction line”

$$\langle x \rangle \approx \frac{v_{dc}}{\alpha r} \quad (25)$$

where the frequency of oscillations (in units of ω_K) satisfies

⁸We will use these terms interchangeably.

$$\Omega \approx \frac{2v_{dc}}{\alpha}, \quad (26)$$

although the theory couldn't tell whether this regime is achieved only for $v_{dc} > 1$ or for lesser currents too. It should be noted that the Walker breakdown current $v_{dc} = 1$ is very high for practical applications. We should note also that the regime of equation (25) is very attractive from an applications point of view because $\alpha r \sim 10^{-6}$, which means the average displacement of the domain wall is 10^6 domain wall lengths Δ for $v_{dc} \sim 1$. Figure 5 shows the average displacement of the domain wall versus the dc-driving current amplitude v_{dc} for different initial conditions⁹. From the plot, we can see that if each solution is calculated with an initial condition $x = 0, \Psi = 0$ at $\tau = 0$ for every value of v_{dc} , then the displacement $\langle x \rangle$ of the domain wall is zero up to $v_{dc} \approx 0.74$. Then $\langle x \rangle$ jumps and stays very close to the theoretical estimate (25) $\langle x \rangle = v_{dc}/(\alpha r)$. On the contrary, if the solutions are calculated with the initial coordinate on the attraction line $x(0) = v_{dc}/(\alpha r)$ (the second condition $\Psi(0) = 0$ seems less important), then the equilibrium solution stays on the attraction line down to $v_{dc} \approx 0.01425$. So we have hysteretic behavior here. Beyond just scientific curiosity, this suggests that we can move the domain wall by a significant distance using a high peak current $v_{dc} > 1$ (above Walker breakdown); to retain the wall at a large distance from its equilibrium position, we can use smaller currents (below 1).

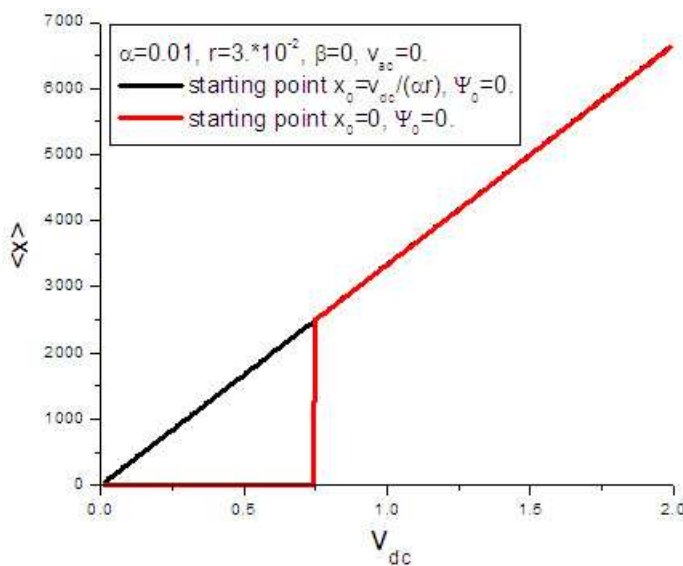


Figure 5: Average displacement $\langle x \rangle$ of a domain wall versus driving dc-current amplitude v_{dc} . $\alpha = 10^{-2}$, $r = 3 \cdot 10^{-2}$, $\beta = 0$, $v_{ac} = 0$ (a) initial point $\Psi(0) = 0$, $x(0) = 0$ – red curve (b) initial point $x(0) = v_{dc}/(\alpha r)$, $\Psi(0) = 0$ – black curve

Figure 6 shows the average coordinate of the wall calculated in the presence of an ac-current. Having in mind that we are interested in practical applications frequency of the current was chosen so, that Shapiro-steps would happen at as low a frequency as possible. For $\Omega = 1.5\pi$, Equation (26) gives $v_{dc} \approx 0.024$ (the graph shows this estimate is surprisingly precise).

Because we have hysteresis, the initial conditions play an important role, so for each curve we will always specify, what initial conditions were used to generate it.

The curve for $\beta = 0$ was generated in the following way. For $v_{dc} = 0.05$ the initial point was taken close to the attraction line.¹⁰ Then the dc-current was adiabatically decreased. The point $v_{dc} \approx 0.0143$ is the smallest current where the attraction line exists. If the dc-current is adiabatically decreased further, then the average coordinate $\langle x \rangle$ abruptly drops to zero. If we don't decrease the current further, but

⁹For this figure we used $r = 3 \cdot 10^{-2}$ (which is large, compared to experimental estimates) because it's easier to analyze, than the case $r = 10^{-4}$. The case $r = 3 \cdot 10^{-2}$ shows richer behavior and it looks easy enough to realize in the experimental setting: increase in r can be achieved by decrease in ω_K , which, in turn, can be realized by making cross section of the wire closer to square.

¹⁰Whenever we use the wording "close to the attraction line", we mean $x(0) = v_{dc}/(\alpha r)$, $\Psi(0) = 0$.

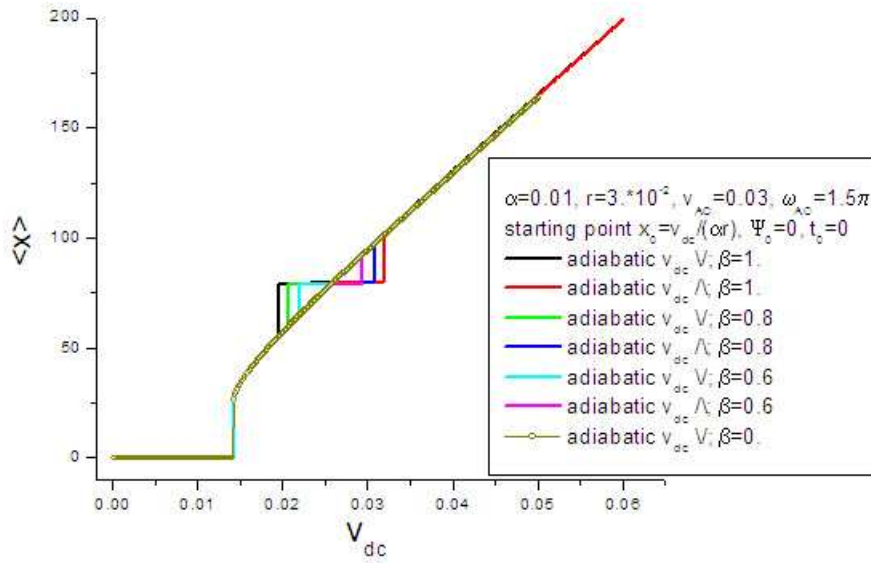


Figure 6: Average displacement $\langle x \rangle$ of a domain wall versus driving dc-current amplitude v_{dc} . $\alpha = 10^{-2}$, $r = 3 \cdot 10^{-2}$, $v_{ac} = 0.03$, $\omega_{ac} = 1.5\pi$, initial point $x(0) = v_{dc}/(\alpha r)$, $\Psi(0) = 0$

adiabatically increase it instead, then $\langle x \rangle$ repeats its behavior and no hysteresis is observed. So we see that it is $\beta \neq 0$, which serves as the source of hysteresis.

More interesting behavior is observed when $\beta \neq 0$. E.g. the black curve is drawn for $\beta = 1$ starting at $v_{dc} = 0.05$ also close to the attraction line. As the dc-current is decreased until $v_{dc} = \Omega\alpha/2$, the $\beta = 1$ -curve almost exactly follows the $\beta = 0$ -curve. Then the mode locking regime occurs and the left half of the Shapiro step is produced. At $v_{dc} \approx 0.0195$, $\langle x \rangle$ abruptly drops to the $\beta = 0$ -curve and then follows it almost exactly¹¹. If we don't decrease v_{dc} below $v_{dc} = 0.0143$, but instead start to increase it again (red curve), then the behavior of the $\beta = 0$ -curve is reproduced almost exactly until $v_{dc} = \Omega\alpha/2$. A further increase leads to a mode locking regime again and the right half of the Shapiro step is reproduced. Further increasing the current causes a sudden end of the mode locking regime at $v_{dc} \approx 0.0318$ after which the curve reproduces the $\beta = 0$ -curve.

The hysteresis observed is illustrated schematically in Fig. 7

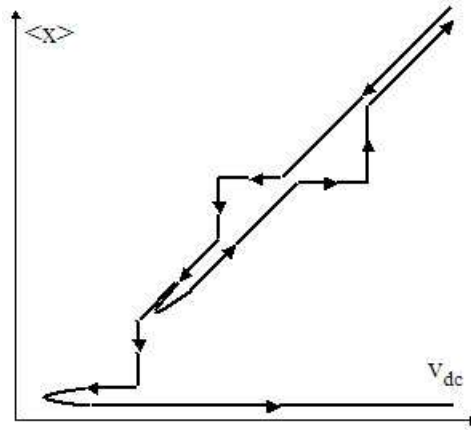


Figure 7: Schematic hysteresis loop for $\alpha = 10^{-2}$, $r = 3 \cdot 10^{-2}$, $v_{ac} = 0.03$, $\omega_{ac} = 1.5\pi$.

Examination of numerical results, shown in Fig. 6 reveals that the width of a Shapiro step is proportional to β :

¹¹The precision of our calculations is not enough to tell whether the difference between curves is due to numerical error.

Step width $\sim \beta$

(27)

and its “left half” width is equal to its “right half” width.

The strength of the mode locking, which is reflected by the width of a Shapiro step, also depends on the ac-current amplitude. Large currents will probably be difficult to realize in experiment (although not necessarily impossible), but we will still consider ac-currents $v_{ac} > 1$. They are worth examining at least because solutions in that case show interesting behavior, which is not observed in Fig. 6. Figure 8 shows the average displacement $\langle x \rangle$ of a domain wall for $v_{ac} = 1.3$. All other parameters are the same except the frequency of the ac-current, which now is taken to be $\omega_{ac} = \pi$. Then relation (26) gives $v_{dc} \approx 0.0157$ for the dc-current, where we expect the Shapiro step to appear. Calculations, depicted in Fig. (8), show that a large value of ac-current allows us to observe the mode locking effect not only when the autogeneration frequency (26) coincides with the ac-current frequency $\Omega = \omega_{ac}$, but also at a multiple frequency 2Ω (corresponding current $v_{dc} = \omega_{ac}\alpha$), and at a fractional frequency $\Omega/2$ (corresponding current $v_{dc} = \omega_{ac}\alpha/4$). All curves, except the yellow one, were generated with initial conditions close to the attraction line for each value of the dc-current. The case of a half-frequency Shapiro step is possible to observe only for $\beta = 1$ (remember, higher β s make the effect more prominent) with a special hysteresis history: we choose the smallest current where the pink, $\beta = 1$ -solution is still non-zero ($v_{dc} \approx 0.0117$) and, instead of using initial conditions close to the attraction line for a smaller current, we adiabatically decrease the current. Under such conditions the mode locking regime persists for a current as low as $v_{dc} \approx 0.0063$

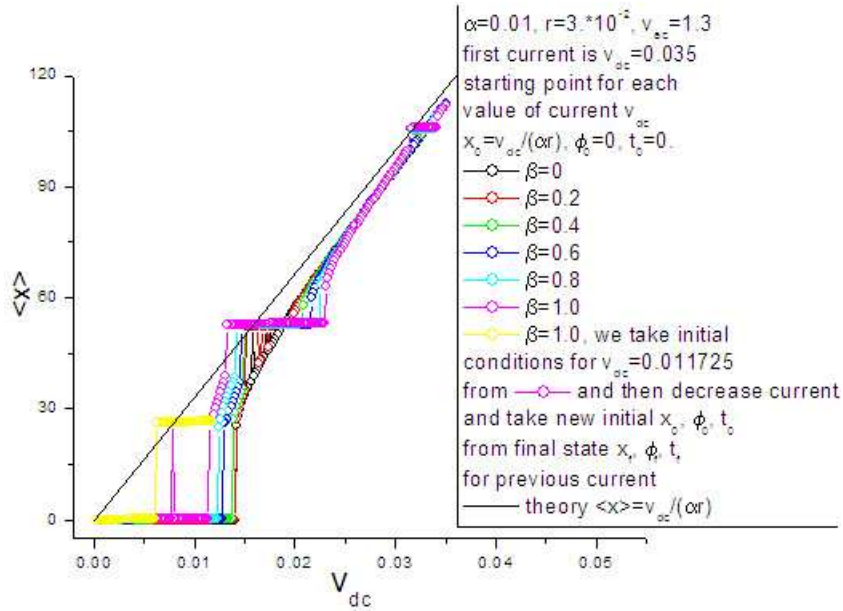


Figure 8: $\alpha = 10^{-2}$, $r = 3 \cdot 10^{-2}$, $v_{ac} = 0.03$, $\omega_{ac} = 1.5\pi$.

4 Quantum mirage effect

Another research project which I was involved in at IBM was a theoretical study of the quantum mirage effect. Let’s describe what the essence of this effect is. The initial quantum mirage experiment was performed by H. Manoharan et.al. [8]. An array of *Co* atoms was arranged on the (111) surface of a single-crystal *Cu* sample. The atoms were arranged so that they formed an ellipse of a given eccentricity e . Then a scanning tunneling microscope (STM) was used to measure the density of states (DOS)¹² on that surface. A *Co* adatom was next placed at one focus of the ellipse and the surface DOS was measured again. Topograph images obtained and their difference are shown¹³ in Figure 9.

¹²Of course, STM measures the density of surface states.

¹³The picture is copied from [9] without a permission

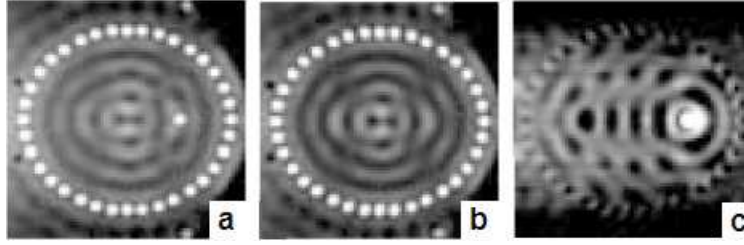


Figure 9: Topograph images inside an elliptic structure made of *Co* adatoms on a *Cu*-surface (a) without a *Co* adatom (b) with a *Co* adatom at the right focus (c) difference (a)–(b). Measurements (a) and (b) are performed at a bias voltage of +10 *mV* of the sample with respect to the STM’s tip.

This experiment was studied theoretically by a few authors ([9], [10], [11], [12]). The most successful theory was an approach suggested by Fiete et. al. [9] based on a single particle scattering theory. In our study of the effect, we had a particular goal – to understand whether the Kondo effect plays an important role in what is seen in experiment. To include Kondo interaction more or less from first principles we needed a more simplified picture.

Some of the experimental results obtained by Manoharan et. al. [8] suggest that the Kondo effect is important to understand the system under consideration. So, it’s natural to apply the Kondo Hamiltonian to study this system.

5 Theoretical description

Let’s briefly review this Hamiltonian. The Kondo Hamiltonian describes the interaction of a localized electron that has a local moment, placed in a sea of itinerant electrons. Such itinerant electrons may be either free ones or in a potential field created, for example, by the ions of a crystal lattice. So, it is the sum of the Hamiltonian of itinerant electrons $T + V$, where T is kinetic energy and V is potential energy of itinerant electrons, and the interaction Hamiltonian H_{int} :

$$H_{Kondo} = T + V + H_{int} \quad (28)$$

The Kondo interaction is [13]

$$H_{int}(\mathbf{R}) = - \sum_{\mathbf{k}, \alpha, \beta} J_{\mathbf{k}\mathbf{p}}(\mathbf{R}) \hat{S}_{\alpha\beta} \hat{c}_{\mathbf{k}\alpha}^\dagger \hat{c}_{\mathbf{p}\beta} \quad (29)$$

where

$$J_{\mathbf{k}\mathbf{p}}(\mathbf{R}) = e^2 \int d^3\mathbf{r}_1 \phi_{\mathbf{k}}^*(\mathbf{r}_1) \phi_L(\mathbf{r}_1 - \mathbf{R}) \int \frac{d^3\mathbf{r}_2}{|\mathbf{r}_1 - \mathbf{r}_2|} \phi_L^*(\mathbf{r}_2 - \mathbf{R}) \phi_{\mathbf{p}}(\mathbf{r}_2) \quad (30)$$

and

$$\hat{S} = \sum_{\alpha\beta} \vec{\sigma}_{\alpha\beta} \hat{c}_{L\alpha}^\dagger \hat{c}_{L\alpha} . \quad (31)$$

In formula (29), $\phi_{\mathbf{p}}(\mathbf{r})$ are the wave functions of the itinerant electrons, constituting some arbitrary orthonormal basis set with eigenvalues \mathbf{p} , $\hat{c}_{\mathbf{p}\alpha}^\dagger / c_{\mathbf{p}\alpha}$ are creation/destruction operators of electrons in states $\phi_{\mathbf{p}}(\mathbf{r})$ with spin z-component α , $\vec{\sigma}_{\alpha\beta}$ is a vector consisting of $\alpha\beta$ components of Pauli matrices

$$\vec{\sigma}_{\alpha\beta} = (\sigma_{x,\alpha\beta}, \sigma_{y,\alpha\beta}, \sigma_{z,\alpha\beta}) , \quad (32)$$

\hat{S} is the spin operator of the impurity electron, $\phi_L(\mathbf{r})$ is a wave function of this localized electron, centered at $\mathbf{r} = 0$ and $\hat{c}_{L\alpha}^\dagger / c_{L\alpha}$ are creation/destruction operators of electrons with spin z-component α in state $\phi_{L\alpha}(\mathbf{r})$. It is assumed that the impurity resides at $\mathbf{r} = \mathbf{R}$.

$J_{\mathbf{k}\mathbf{p}}$ is called an exchange integral and to do specific calculations using formula (29) we need to know an explicit expression for impurity wave function $\phi_L(\mathbf{r})$. The situation simplifies if it is assumed that the magnetic impurity is “small” in the sense that $\phi_{\mathbf{p}}(\mathbf{R} + \Delta\mathbf{r}) \approx \phi_{\mathbf{p}}(\mathbf{R})$ for $|\Delta\mathbf{r}| < r_{imp}$, where r_{imp} is the decay length of the impurity wave function $\phi_L(\mathbf{r})$. Then, H_{int} simplifies to

$$H_{int}(\mathbf{R}) = -J \sum_{\mathbf{k}\mathbf{p}, \alpha\beta} \phi_{\mathbf{k}}^*(\mathbf{R}) \phi_{\mathbf{p}}(\mathbf{R}) \tilde{S}_{\alpha\beta} \hat{c}_{\mathbf{k}\alpha}^\dagger \hat{c}_{\mathbf{p}\beta} \quad (33)$$

$$J = e^2 \int d^3\mathbf{r}_1 \phi_L(\mathbf{r}_1) \int \frac{d^3\mathbf{r}_2}{|\mathbf{r}_1 - \mathbf{r}_2|} \phi_L^*(\mathbf{r}_2)$$

In this approximation, instead of an entire function $\phi_L(\mathbf{r})$, only a single fitting parameter J is needed to write H_{int} .¹⁴

Now, it should be understood, that the assumption, that the wave functions $\phi_{\mathbf{p}}(\mathbf{r})$ can be considered constant along the size of impurity, cannot be satisfied for all wave functions in any full set of orthonormal functions, because the higher the energy of an electron, the faster the spatial oscillations of the wave function. But it also should be understood, that a scanning tunneling microscope probes only a limited energy window and it’s sensible to assume, that if in that energy window wave functions $\phi_{\mathbf{p}}(\mathbf{r})$ can be considered constant along the length of the impurity, then it will be a reasonable approximation.

Here it’s time for a short digression from theory to experiment. As [14] states “electrons occupying surface states on the close-packed surfaces of noble metals form a two-dimensional nearly free electron gas” (see also references in [14]). That means that 2D plane waves, described by a wave vector \mathbf{k} , are a good wave function basis for describing the surface electrons on a *Cu* surface. Using measurements in [14], where the wave number k was calculated for various bias voltages, we find that for a bias voltage $-0.3 V$ (electrons with energy $-0.3 eV$ with respect to the Fermi energy), the wavelength is $\lambda \approx 52.4 \text{ \AA}$ and for a bias voltage $0.3 V$, the wavelength is $\lambda \approx 24.2 \text{ \AA}$. Various methods of calculations and measurements of the *Co*-atom radius found in literature all give values $r_{atom} < 2 \text{ \AA}$ (see [15], [16]), therefore, we conclude that the approximation of a strongly localized impurity is reasonable here.

We choose the functions $\phi_{\mathbf{p}}(\mathbf{r})$ to be eigenfunctions of the “free” Hamiltonian (without the Kondo interaction part). Here another approximation comes in. We assume that the *Co* adatoms create an impenetrable potential barrier for the electrons. This means, that in order to find basis set functions we had to solve the 2D Schrödinger equation for a particle in an elliptic box. This is easier to do in elliptic coordinates

$$\begin{aligned} x &= t \cosh u \cos v \\ y &= t \sinh u \sin v \end{aligned} \quad (34)$$

where $u \in [0, +\infty)$, $v \in [0, 2\pi)$ are new elliptic coordinates and t is an arbitrary parameter. If we choose

$$\begin{aligned} t &= \sqrt{a^2 - b^2} \\ u_b &= \operatorname{arctanh}(b/a) \end{aligned} \quad (35)$$

where a and b are the semi-axes of some ellipse $x^2/a^2 + y^2/b^2 = 1$, then the points

$$\begin{aligned} u &\in [0, u_b] \\ v &\in [0, 2\pi) \end{aligned} \quad (36)$$

¹⁴Note, that when formula (33) is used for a plane wave basis $\phi_{\mathbf{p}}(\mathbf{r}) = \exp(i\mathbf{p}\mathbf{r}/\hbar)/\sqrt{N}$ it gives $H_{int} = -\frac{J}{N} \sum_{\mathbf{k}\mathbf{p}, \alpha\beta} \exp[-i\mathbf{R}_j(\mathbf{k} - \mathbf{p})/\hbar] \tilde{S}_{\alpha\beta} \hat{c}_{\mathbf{k}\alpha}^\dagger \hat{c}_{\mathbf{p}\beta}$, which differs from the result in [13] by a minus sign in the exponent. The reason is that [13] implicitly uses a tight binding approach, for details see **Appendix A**.

cover the area of this ellipse.

The Schrödinger equation

$$\begin{aligned}\Delta\phi + k^2\phi &= 0 \\ k^2 &= \frac{2m^*E}{\hbar^2},\end{aligned}\tag{37}$$

with E the energy of the electron, is transformed to

$$\frac{1}{t^2(\sinh^2 u + \sin^2 v)}\left(\frac{\partial^2\phi}{\partial^2 u} + \frac{\partial^2\phi}{\partial^2 v}\right) + k^2\phi = 0\tag{38}$$

in elliptic coordinates. Separation of variables shows [17], that the solution to equation (38) can be written in terms of special functions, the elliptic cosine $ce_m(q, v)$, which is an even function with respect to the variable v , and the elliptic sine $se_m(q, u)$, which is an odd function with respect to u :

$$\begin{aligned}\psi_m(q, u, v) &= \frac{1}{|\psi_m(q)|} Se_m(q, u)se_m(q, v) \\ \phi_m(q, u, v) &= \frac{1}{|\phi_m(q)|} Ce_m(q, u)ce_m(q, v)\end{aligned}\tag{39}$$

where $|\psi_m(q)|$ and $|\phi_m(q)|$ are the absolute values of corresponding functions¹⁵ and q is

$$q = \frac{1}{4} k^2 t^2.\tag{40}$$

These functions are implemented numerically using Mathieu functions:

$$\begin{aligned}se_m(q, v) &= S(b_m(q), q, v) \\ ce_m(q, v) &= C(a_m(q), q, v)\end{aligned}$$

where $C(a, q, v)$, $S(b, q, v)$ are even and odd Mathieu functions, m is an integer, $a_m(q)$ and $b_m(q)$ are characteristic functions, which guarantee that for a given value of q , the functions $C(a_m(q), q, v)$ and $S(b_m(q), q, v)$ are 2π -periodic in v .¹⁶ The functions Se and Ce are called the elliptic sine and elliptic cosine of an imaginary argument¹⁷:

$$\begin{aligned}Se_m(q, u) &= S(-ib_m(q), q, iu) \\ Ce_m(q, u) &= C(a_m(q), q, iu).\end{aligned}$$

Besides solving the noninteracting Schrödinger equation (37), we have to satisfy the boundary condition

$$\begin{aligned}\phi_m(u_b, v) &\equiv 0 \\ \psi_m(u_b, v) &\equiv 0\end{aligned}$$

or equivalently

$$\begin{aligned}Se_m(q, u_b) &= 0 \\ Ce_m(q, u_b) &= 0\end{aligned}\tag{41}$$

¹⁵Absolute values are defined in a usual manner through the scalar product $|f| = \sqrt{\langle f|f \rangle}$

¹⁶For details see, for example, [17] or [18].

¹⁷Despite their appearance they are real valued functions.

which says that we assume an infinite strength potential wall. Solving equations (41), gives us a discrete spectrum of energies for the system. For given values m and u_b , these equations have an infinite number of roots. Let's denote the solutions of the Se -equations as $q_n^s(m, u_b)$ and the solutions of the Ce -equations as $q_n^c(m, u_b)$ where n is a natural number, which numbers the solutions of equations (41) for given m and u_b :

$$\begin{aligned} Se_m(q_n^s(m, u_b), u_b) &\equiv 0 & \forall n, m, u_b \\ Ce_m(q_n^c(m, u_b), u_b) &\equiv 0 & \forall n, m, u_b . \end{aligned}$$

Then, using (40), the energy levels are

$$\begin{aligned} E_{m,n}^s(u_b) &= E^* q_n^s(m, u_b) \\ E_{m,n}^c(u_b) &= E^* q_n^c(m, u_b) \\ E^* &= \frac{2\hbar^2}{m^* t^2} . \end{aligned} \quad (42)$$

Once again, here E^s are the energy levels corresponding to sine wave functions in (39), and energy levels E^c correspond to cosine wave functions. Parameters t and u_b are given by relations (35). When m is fixed, n is good for numbering the energy levels E^s or E^c in increasing order, but for the whole collection $E_{m,n}^s, E_{m,n}^c$ neither m nor n nor the pair (m, n) is good for numbering, so after the energy levels are found numerically, they are placed in order and assigned a new index.

In elliptic coordinates (34), the scalar product of functions $f(u, v)$ and $g(u, v)$ defined inside the ellipse (36) is expressed as

$$\langle f|g \rangle = \frac{t^2}{2} \int_0^{u_b} du \int_0^{2\pi} dv f^*(u, v)g(u, v)(\cosh 2u - \cos 2v) \quad (43)$$

The eigenfunctions in Eq. (39) automatically turn out to be orthogonal for values of q found according to (41)

$$\begin{aligned} \langle \psi_m(q_n^s(m, u_b)) | \psi_b(q_a^s(b, u_b)) \rangle &\propto \delta_{na}\delta_{mb} \\ \langle \phi_m(q_n^c(m, u_b)) | \phi_b(q_a^c(b, u_b)) \rangle &\propto \delta_{na}\delta_{mb} \\ \langle \psi_m(q_n^s(m, u_b)) | \phi_b(q_a^c(b, u_b)) \rangle &= 0 , \end{aligned}$$

and the absolute values in the solutions (39) can now be expressed as

$$|\psi_m(q_n^s(m, u_b))|^2 = \frac{t^2}{2} \int_0^{u_b} du \int_0^{2\pi} dv Se_m^2(q_n^s(m, u_b), u) se_m^2(q_n^s(m, u_b), v)(\cosh 2u - \cos 2v) \quad (44)$$

$$|\phi_m(q_n^c(m, u_b))|^2 = \frac{t^2}{2} \int_0^{u_b} du \int_0^{2\pi} dv Ce_m^2(q_n^c(m, u_b), u) ce_m^2(q_n^c(m, u_b), v)(\cosh 2u - \cos 2v) . \quad (45)$$

Let's introduce a common notation for the sine and cosine eigenfunctions (we omit the dependence of wave functions on u_b to simplify our crowded notations a little bit):

$$\chi_{mni}(u, v) = \begin{cases} \psi_m(q_n^s(m, u_b), u, v), & \text{if } i = 0; \\ \phi_m(q_n^c(m, u_b), u, v), & \text{if } i = 1 \end{cases} \quad (46)$$

$$E_{mni} = \begin{cases} E_{m,n}^s(u_b), & \text{if } i = 0; \\ E_{m,n}^c(u_b), & \text{if } i = 1 \end{cases} . \quad (47)$$

Then the one particle part of the Hamiltonian (28) can be written as

$$H_{Kondo}(\mathbf{R}) = \sum_{mni,\alpha} E_{mni} c_{mni,\alpha}^\dagger c_{mni,\alpha} - J \sum_{mni,baj,\alpha\beta} \chi_{mni}(\mathbf{R}) \chi_{baj}(\mathbf{R}) \hat{S}_{\alpha\beta}^z \hat{c}_{mni,\alpha}^\dagger \hat{c}_{baj,\beta} \quad (48)$$

where $c_{mni,\alpha}^\dagger/c_{mni,\alpha}$ are creation/destruction operators of states $\chi_{mni}(u, v)$ (46) with spin z-component α ; by \mathbf{R} we denote the position of magnetic impurity and we used formula (33).

6 Matching experiment

Now we are in a position to discuss specific experimental data. Experiment shows [14], that the surface plane waves, mentioned in Section 5, at $k = 0$ have energy E_0 with respect to the bulk Fermi energy of copper and $E_0 = -0.44 \pm 0.01$ eV. So, the bottom of the surface band lies below the Fermi energy. Surface electrons have an effective mass $m^* \approx 0.38m_e$.

Let's consider an ellipse made of *Co*-adatoms (see [9]) with $a = 71.3$ Å and eccentricity

$$\epsilon = \sqrt{1 - \frac{b^2}{a^2}} = 0.5 \quad (49)$$

That gives $t \approx 35.7$ Å, $u_b \approx 1.32$, energy “unit” (42) $E^* \approx 5.06 \cdot 10^{-21} J \approx 31.6$ meV. Table 1 shows eigenfunctions with corresponding energies (42) (sorted in increasing order) calculated by numerically solving equations (41).

One goal of our calculations is to find the density of states of this “quantum corral” structure. When the energy spectrum is discrete, the density of states is a sum of δ -functions:

$$\rho(\mathbf{r}, E) = \sum_n |\varphi_n(\mathbf{r})|^2 \delta(E - E_n) \quad (50)$$

where $\varphi_n(\mathbf{r})$ are eigenfunctions of a system. The spatial densities of states $|\varphi_n(\mathbf{r})|^2$ for the first 72 energy levels in the corral are shown in Figure (10).

Let's return to figure (9), which we started our discussion from. When topograph images are taken, the height of the STM's tip above the sample surface, which is needed to maintain constant tunneling current, is measured. This current is proportional to the densities of states both in the sample and the tip and to the transparency of the potential barrier between them¹⁸:

$$I(\mathbf{r}) \propto \rho_t(E_F) \int_0^{eV} T(E_F + \epsilon) \rho_c(\mathbf{r}, E_F + \epsilon) d\epsilon, \quad (51)$$

where $T(\epsilon)$ is the transparency of the potential barrier between the sample and the tip and $\rho_c(\mathbf{r}, \epsilon)$ is the density of states inside the corral; these are the states where electrons from the STM's tip go (for positive bias V). Relation (51) has some assumptions inside, which need further explanation. It assumes that the density of states in the tip can be approximated by the constant $\rho_t(E_F)$ within the interval $\epsilon \in (E_F, E_F + eV)$. This is indirectly verified by the experiment [8], where the topograph images didn't depend on the material the tip was made of. The transparency of the potential barrier in the quasi-classical (WKB) approximation is given by the expression (see [19])

$$T(\epsilon) \propto \exp\left(-\frac{2}{\hbar} \int_{a(\epsilon)}^{b(\epsilon)} \sqrt{2m(u(x) - \epsilon)} dx\right) \quad (52)$$

where the potential barrier profile is given by the function $u(x)$ and the integration is performed over the classically inaccessible region. We are going to make another assumption, which we won't prove rigorously. Namely, we will assume that $T(\epsilon)$ can be approximated by the constant $T(E_F)$ in the interval $\epsilon \in (E_F, E_F + eV)$. Then equation (51) becomes

¹⁸As in [8] and [9] the bias V across the tunnel junction is the voltage of the sample measured with respect to the tip.

Table 1: Shown are a few eigenfunctions, ordered according their energies for a 2D ellipse with semi-axis $a = 71.3 \text{ \AA}$ and eccentricity $\epsilon = 0.5$. (u, v) are elliptic coordinates according to Eq. (34) with $t = \epsilon a$. Note that these functions need to be normalized before using them in calculations.

Level number	Energy, meV	Wave function
1	0.013	$Ce_0(q, u)ce_0(q, v)$
2	0.031	$Ce_1(q, u)ce_1(q, v)$
3	0.036	$Se_1(q, u)se_1(q, v)$
4	0.057	$Ce_2(q, u)ce_2(q, v)$
5	0.061	$Se_2(q, u)se_2(q, v)$
...
40	0.413	$Se_6(q, u)se_6(q, v)$
41	0.419	$Ce_1(q, u)ce_1(q, v)$
42	0.448	$Ce_4(q, u)ce_4(q, v)$
43	0.452	$Se_1(q, u)se_1(q, v)$
44	0.466	$Se_4(q, u)se_4(q, v)$
45	0.472	$Ce_{10}(q, u)ce_{10}(q, v)$
46	0.472	$Se_{10}(q, u)se_{10}(q, v)$

$$I(\mathbf{r}) \propto T(E_F) \int_0^{eV} \rho_c(\mathbf{r}, E_F + eV) dV \quad (53)$$

We have found that inside the corral structure (to be more precise, within our approximation of impenetrable walls) only discrete levels within Cu surface state band are allowed. So, instead of (53) we will have

$$I(\mathbf{r}) \propto T(E_F) \sum_{E_F < E_i < E_F + eV} \rho_c(\mathbf{r}, E_i) \quad (54)$$

Topograph images are taken in the constant current mode. In this mode, the height of the tip is adjusted in order to retain a constant tunneling current $I(\mathbf{r}) \equiv I$. To extract the height of the tip for a microscope, operating in the constant current mode, from the equation (53) or (54) we will need to use the Simmons formula [20] for calculating the integral in the relation (52):

$$\int_{x_1}^{x_2} \sqrt{f(x)} dx \approx \sqrt{\bar{f}} (x_2 - x_1) \quad (55)$$

where $\bar{f} = \frac{1}{x_2 - x_1} \int_{x_1}^{x_2} f(x) dx$.

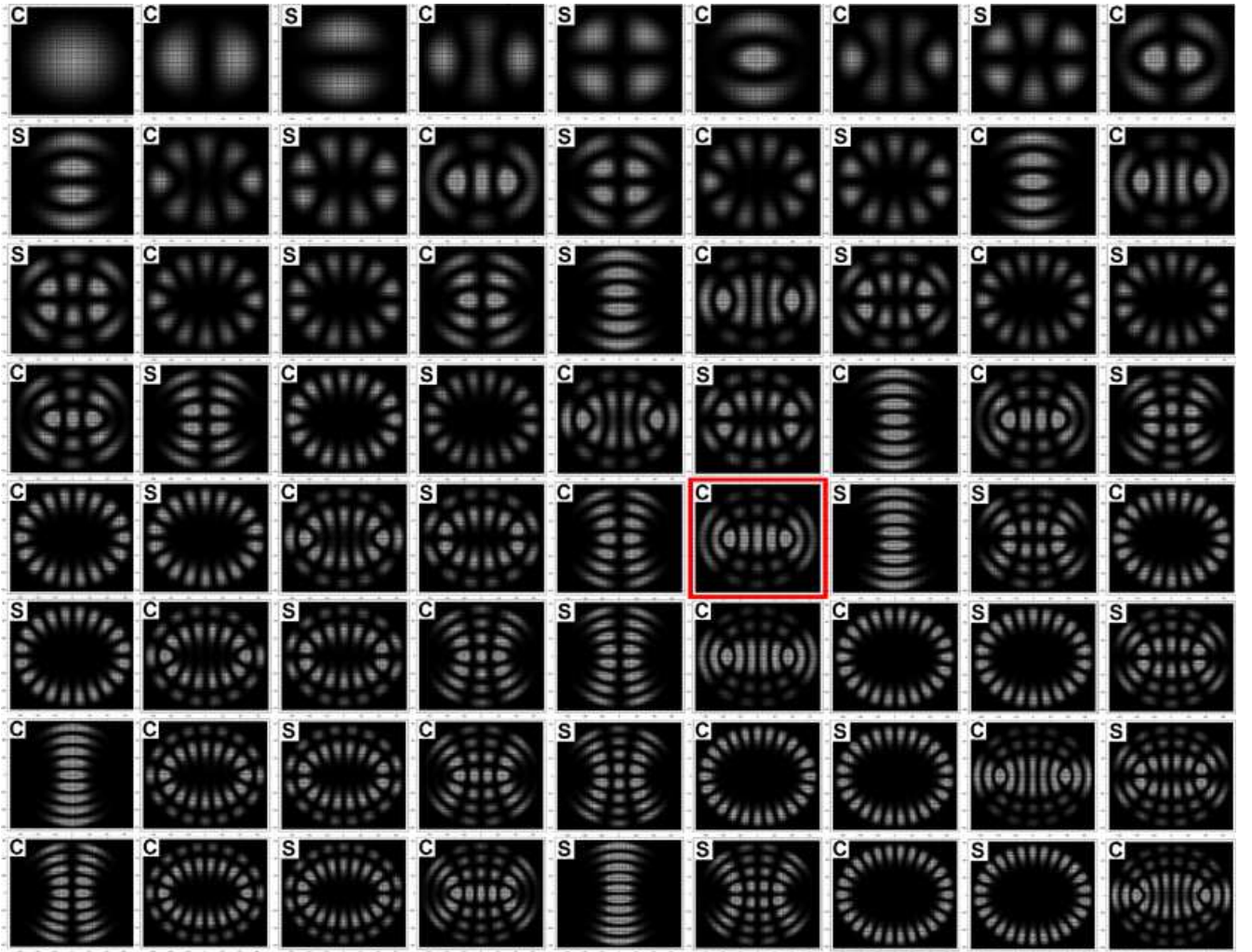


Figure 10: Spatial densities of states for first 72 energy levels in the elliptic structure with major semi-axis $a \approx 71.3\text{\AA}$ and eccentricity $e = 0.5$. Energy increases from left to right and then top-down. Labels in upper-left corners show whether it's a sine or a cosine state. Red square shows the 42nd state with $E \approx 0.448\text{ eV}$. Measurements of copper surface bandwidth (BW) give $BW = 0.44 \pm 0.01\text{ eV}$, so this is the closest to Fermi energy level.

We denote by d the distance between the tip and the copper surface. The Simmons formula allows us to find a pretty precise approximation for the transparency of the tunnel barrier:

$$T(\epsilon, d) \propto \exp\left(-\frac{2}{\hbar} \sqrt{2m(\bar{u}(d) - \epsilon)} d\right). \quad (56)$$

We have written $T(\epsilon, d)$ as a function of the distance d as well as the energy ϵ here because the form of the potential energy $u(x)$ depends on the distance d . Substituting (56) into (54) we find

$$d \propto \frac{\hbar}{2\hat{p}(d, \epsilon)} \left(\ln\left(\sum \rho_c(\mathbf{r}, E_i)\right) - \ln I \right) \quad (57)$$

where $\hat{p}(d, \epsilon)$ is defined as

$$\hat{p}(d, \epsilon) = \sqrt{2m(\bar{u}(d) - \epsilon)}. \quad (58)$$

The last assumption we are going to use is that $p(d, E_F)$ can be approximated by a constant \hat{p} for the range of distances d encountered in the experiment. This one is most difficult to prove to be true and

the only confirmation we have is a posterior agreement between our results and the experiment.

Finally, we have to take into account two peculiarities of the images. First of all, a constant background is always subtracted from the image data.¹⁹ This means that for each image a pixel with the minimum intensity is found and it is taken as the black level. The pixel with maximum intensity is considered to be white. That is not something done by hand, it is what the imaging software does when it depicts a 2-dimensional numerical array. Therefore when we are discussing images, we can omit the constant term $\ln I$ as well as the “assumed to be constant” factor $\hbar/(2\hat{p})$ in (57). The second peculiarity is that if we are to create an image of a two dimensional data set $Z(x, y)$, then images plotted using $\ln Z(x, y)$ look indistinguishable from images plotted using $Z(x, y)$ itself. So, we can conclude that for simulating topograph images we can plot

$$\sum_{E_F < E_i < E_F + eV} \rho_c(\mathbf{r}, E_i) . \quad (59)$$

To include the effect of the atomic DOS of the Co atoms making up the corral, we add the function

$$\rho_{at}(\mathbf{r}) = Y \left[1 - \frac{1}{R_{at}^2} (\mathbf{r} - \mathbf{r}_c)^2 \right] \quad (60)$$

to (59), where fitting parameters \mathbf{r}_c – the position of the atom, R_{at} – the atom radius, and Y – image brightness, serve to reach agreement with experiment (Fig. 9). This means that for simulating topograph images we have to plot d_{imag} :

$$d_{imag} \equiv \rho_{at}(\mathbf{r}) + \sum_{E_F < E_i < E_F + eV} \rho_c(\mathbf{r}, E_i) \quad (61)$$

Let’s examine the energy levels in Table 1. The bulk Fermi energy of copper is $E_F \approx 0.44$ eV. The topograph images in the experiments [8] are taken for bias $V = 0.01$ V. Then the only energy level belonging to the interval $(E_F, E_F + eV)$ is the level $n = 42$. By comparing the density of states for this level in Fig. 10 to the topograph image in Fig. 9(b) we see that they do not match. The second guess would be that the next level $n = 43$ – or may be even higher levels – contributes too. Fig. 11 shows 2D-plots of the function (61) where higher levels are accounted for.

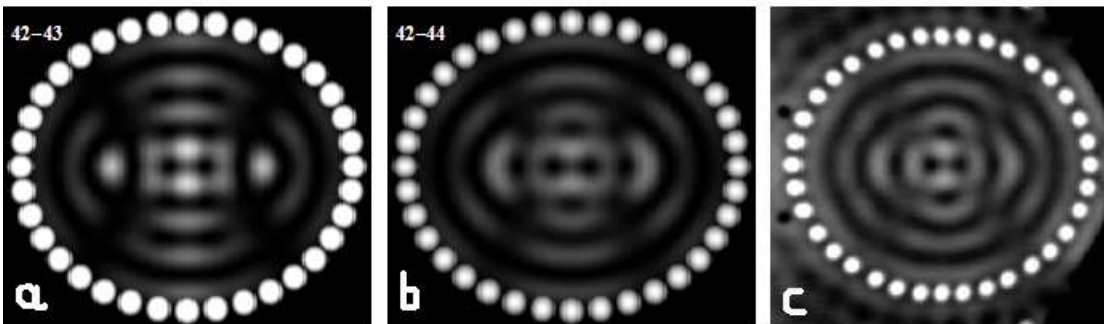


Figure 11: Calculated d_{imag} using (a) levels 42 and 43 (b) levels 42, 43 and 44 (c) experimental topograph image from [8]. Brightness Y of the atomic states was adjusted to give best agreement with experiment in figure (b).

From Fig. 11 we see, that the best agreement with experiment is achieved when (61) is calculated using levels #42 – 44. Here some explanations are in place why we include levels, which, for the bias voltage of 10 mV should not contribute to the tunnel current. The reason for that is a limitation of our approach, where we assume that atoms, making up the corral structure, create an impenetrable potential barrier. In reality, this barrier is far from impenetrable. If instead we consider the potential well with large but finite wall width and strength, we will discover that energy levels (a) broaden and (b) shift; the energy spectrum becomes continuous. Out of these two processes – the level broadening – will definitely lead to the fact, that wave functions other than #42 will contribute their density of

¹⁹Even if it wasn’t, the constant background is usually subtracted from experimental data.

states to the region $\epsilon \in (E_F, E_F + eV)$. Of course, these wave functions will differ from the ones found in our model, but as we can see in Fig. 11 even the crudest approximation given by the expression (61) works pretty well.

Now let's see what happens to the topograph picture when we add a Co atom at one focus of the ellipse. The inclusion of the atom has two effects: it creates a Coulomb potential barrier and also interacts with electrons via the Kondo term in the Hamiltonian (48).

First we consider what happens to eigenstates within our model, and then we argue how our conclusions for the model relate to the reality of the experiment.

To account for potential barrier, we need to find new eigenstates in the elliptic well with a point (or may be finite) potential hill at a focus. The problem with this approach is that potential at a single focus is not consistent with the elliptic coordinates we chose. So, we will have to do some handwaving. Let's consider a very high potential of a small size. It is understood that eigenfunctions will have to vanish at this focus. But we know that sine solutions in (39) have the zero amplitude anyway. So, we can make an important conclusion that sine solutions remain unaffected by the presence of an atom at the focus.

Cosine solutions are more difficult to treat. As we have already said the placement of the atom at the focus destroys the symmetry of the elliptical coordinate system. This means that the separation of variables is not possible anymore and consequently we can't give an answer in general (the analytic one; numerical solution is, of course, still possible). But we can make some analogies. It can be shown analytically that if, instead of an ellipse, we consider a circle barrier with an impenetrable potential (not just a δ -function, but something more intense) in the center, then the only state having non-zero amplitude in the center (the state with angular momentum $l = 0$) vanishes. So, we can speculate that a very strong point barrier removes DOS at its position (meaning that it removes all states which have a non-zero amplitude at the position of the potential).

Out of states #42 – 44 only states #43 and 44 are sine states, so only they will contribute to d_{imag} in (61). Fig. 12 shows the result of such a calculation.

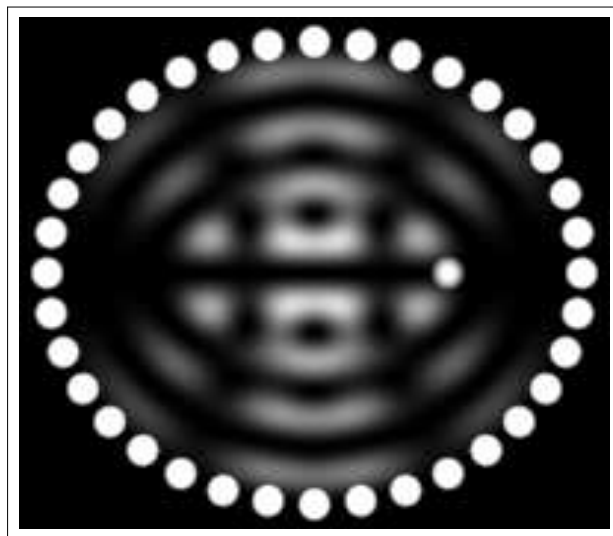


Figure 12: Calculated d_{imag} using levels 43 and 44.

There is still a problem here. The experimental topograph image with the Co atom at the focus (see Fig. 9(a)), which the image in Fig. 12 is expected to reproduce, looks identical to the experimental topograph image without the atom. Our d_{imag} in Fig. 12, on the contrary, doesn't look like the image in Fig. 11(b). We will discuss this disagreement later.

Finally we calculate the difference of the topograph images, the image with the Co atom at the focus – the image without the atom, to reproduce Fig. 9(c). The result is shown in Fig. 13. Also shown is the topograph picture taken from experiment. We can call the agreement between them satisfactory. Let's return to the problem that the simulated topograph image in Fig. 12 doesn't look similar to

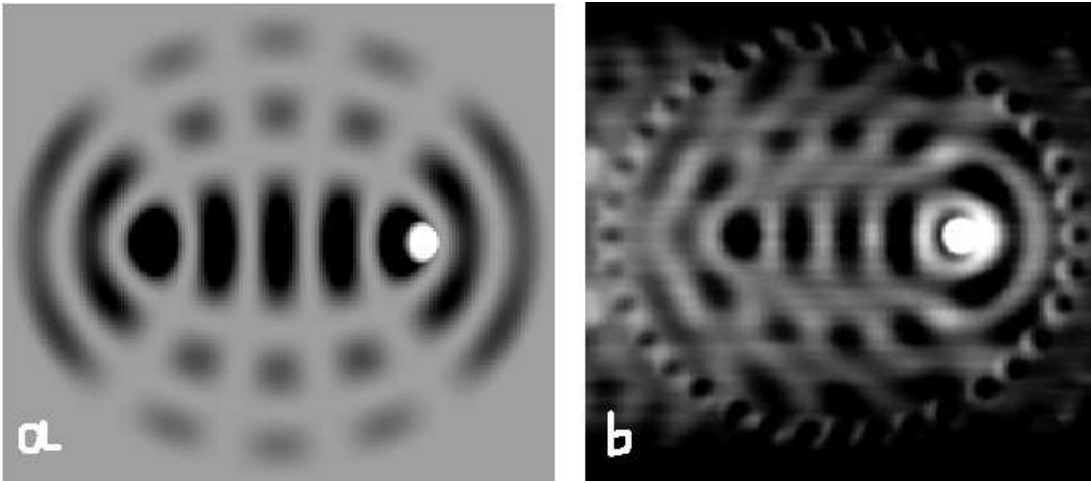


Figure 13: Comparison of the difference of topographic images with and without the Co atom at the right focus (a) calculated $\rho_{at} - \rho_{42}$ (b) experimental [9].

the measured topograph in Fig. 9(a). The source of this distinction is our assumption of an infinitely high barrier (to prohibit levels with non-zero amplitude at the ellipse focus the potential should be stronger than a delta-function). In the opposite limit of a very weak potential, we can treat the problem perturbatively. We can see that the measured topograph with the cobalt atom at the right focus is all but indistinguishable from the measured topograph with the atom. So, the experiment tells us that the case of the weak potential is indeed realized. This conclusion makes our whole approach, where we consider the potential created by Co atoms making up the wall impenetrable, very questionable. But let's proceed. In the first order perturbation theory, new eigenfunctions and eigenenergies are given by formulas [19]:

$$\begin{aligned}\tilde{\varphi}_n(\mathbf{r}) &= \varphi_n(\mathbf{r}) + \sum_{m \neq n} \frac{V_{mn}}{E_n - E_m} \varphi_m(\mathbf{r}) \\ \tilde{E}_n &= E_n + V_{nn}\end{aligned}\quad (62)$$

where V_{mn} are matrix elements of the perturbing potential (the Co atom potential) between unperturbed eigenstates $|m\rangle$ and $|n\rangle$:²⁰

$$V_{mn} = \langle m | \hat{V} | n \rangle . \quad (63)$$

The simplest case to analyze is when the Co atom at the focus creates a delta-function potential:

$$V(\mathbf{r}) = V_0 \delta(\mathbf{r} - \mathbf{R}) \quad (64)$$

where \mathbf{R} points at the focus with the adatom. The matrix elements (63), the perturbed eigenfunctions and energies (62) then become²¹

$$\begin{aligned}V_{mn} &= V_0 \varphi_m(\mathbf{R}) \varphi_n(\mathbf{R}) \\ \tilde{\varphi}_n(\mathbf{r}) &= \varphi_n(\mathbf{r}) + V_0 \varphi_n(\mathbf{R}) \sum_{m \neq n} \frac{\varphi_m(\mathbf{R})}{E_n - E_m} \varphi_m(\mathbf{r}) \\ \tilde{E}_n &= E_n + V_0 \varphi_n^2(\mathbf{R})\end{aligned}\quad (65)$$

All sine eigenfunctions are zero at the ellipse foci, so they are not affected by the perturbing delta-potential at all (in all orders of perturbation theory). They also don't contribute to the sum in (65)

²⁰By $|n\rangle$ or $\varphi_n(\mathbf{r})$ we denote eigenfunctions (46) numbered using a single index n .

²¹Remember that all eigenfunctions are real valued.

when we calculate the perturbed cosine eigenfunctions. This means that the addition of an adatom at the focus leaves states #43 and 44 intact (along with corresponding densities of those states) and the perturbed density of the state #42 will be

$$\tilde{\rho}_{42}(\mathbf{r}) = \tilde{\varphi}_{42}^2(\mathbf{r}) = \tilde{\rho}_{42}(\mathbf{r}) + 2V_0\varphi_n(\mathbf{r})\varphi_n(\mathbf{R}) \sum_{m \neq n} \frac{\varphi_m(\mathbf{R})}{E_n - E_m} \varphi_m(\mathbf{r}) + O(V_0^2). \quad (66)$$

For small V_0 , Fig. 11(b) will stay the same, although the difference of topograph images with and without Co atom $d_{imag}(\text{Co}) - d_{imag}(\text{no Co})$, will now be given by the relation

$$d_{imag}(\text{Co}) - d_{imag}(\text{no Co}) = 2V_0\varphi_n(\mathbf{r})\varphi_n(\mathbf{R}) \sum_{m \neq n} \frac{\varphi_m(\mathbf{R})}{E_n - E_m} \varphi_m(\mathbf{r}) + O(V_0^2) \quad (67)$$

It's hardly possible to say now what the image produced using (67) will look like only by looking at the formula. A 2D-plot of the function (67) is shown in Fig. 14. Also shown is the corresponding image from Fig. 9(c), which was measured in experiment.

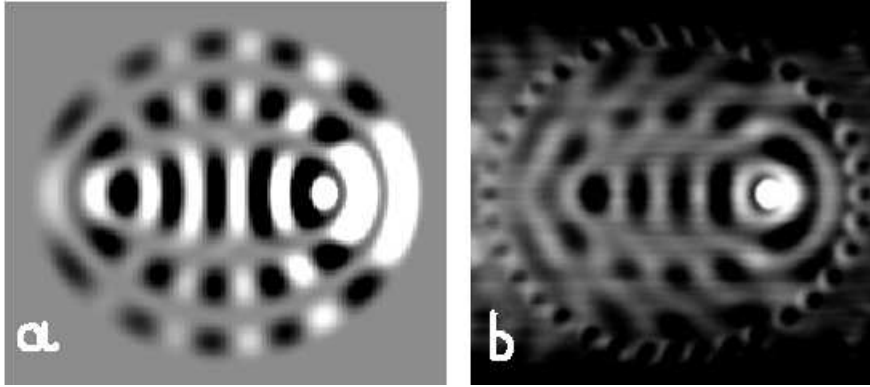


Figure 14: The difference of topographic images with and without a Co atom at the right focus (a) plotted using the formula (67) [perturbation theory approach, $V_0 < 0$] (b) taken in experiment [9].

We see that the similarity between the two plots (experimental and simulated) is much better than in Fig 13. Only the rightmost part of our picture, between the focus with the adatom and the boundary is quite different from the experimental result. This is something we cannot explain within our model. The picture shown was obtained for $V_0 < 0$ (again, for imaging relation (67) the magnitude of V_0 doesn't matter). The change of the sign of V_0 leads to change of black to white and vice versa. So, our results tell us that if the potential scattering is the main source of the effects observed, then the Co atoms create an attractive potential.

Now, remember that up to this point we didn't take into account any effects caused by the Kondo term in the Hamiltonian (48). Therefore it looks appropriate to conclude that even potential scattering without taking into account the Kondo effect can reproduce many features seen in experiment. The disadvantage of our approach – discrete energy levels – doesn't allow us to study the spectroscopic measurements dI/dV , so this is all we can do with the potential scattering effects.

The Kondo part is more difficult to treat theoretically, even with handwaving type of arguments. Therefore let's turn to the experimental evidence, which shows that when a Kondo atom is placed at the copper surface the density of surface states is suppressed to zero at the Fermi energy at the position of the atom. We can rephrase this by saying that the Kondo atom prohibits the states around the Fermi energy with a non-zero amplitude at the position of the atom. It is a very liberal explanation, but if we accept it we will see, that the Kondo atom acts in the same way as an impenetrable potential barrier. If a particular state has zero amplitude at the position of the Kondo atom, then the Hamiltonian (48) says that this state and the atom will not interact at all. So, sine states will not be perturbed by

the Kondo atoms, while the cosine states will. Such extremely simplified approach leads again to the Fig. 13.

Unfortunately we didn't succeed in performing precise (numerical renormalization group) calculations applied to the corral eigenstates $\varphi_n(\mathbf{r})$ which initially was the goal of our approach.

Finally, let's address an issue, which we have with explaining experimental results. As we saw it is possible to model topograph images satisfactorily even without the notion of the Kondo interaction. But the experiment didn't observe the images discussed here if the Kondo atom at the focus (Co or Fe) was replaced by a non-Kondo atom (at least for the CO-molecule, which was tried). May be this is indeed a proof that the potential scattering is irrelevant. Yet another possible explanation is that the Kondo interaction leads to an effective potential scattering of surface electrons. One of possible mechanisms is the well-known fact that the Kondo atoms create excess of the charge around them. It is possible to say that the accumulation of the electronic charge is a sign of an effective attractive potential.

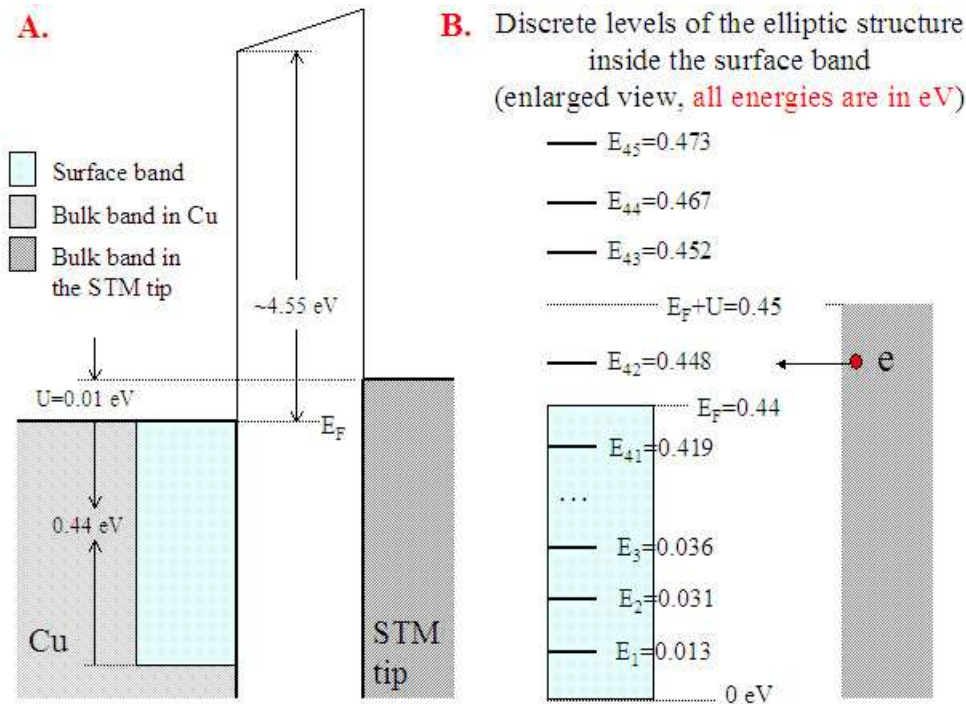


Figure 15: (a) Schematic picture of the experimental setup (b) Calculated energy levels for the elliptic structure together with experiment conditions.

7 Acknowledgements

I thank Dr. Barbara Jones for being my host and advisor during the apprenticeship at the Almaden Center. I also thank my advisor, Prof. Jim Freericks for reviewing this report. Special thanks go to Prof. Wesley Mathews for his invaluable help with Mathematica.

This work was supported by the National Science Foundation under Grant No. DMR-0210717 and by the Office of Naval Research under Grant No. N00014-99-1-0328.

References

- [1] Martyn Williams and Paul Kallender. *China's Lenovo to buy IBM's PC business*. InfoWorld. http://www.infoworld.com/article/04/12/07/HNlenovoibm_1.html.

- [2] L. D. Landau and E. M. Lifshits. *Electrodynamics of Continuous Media*. Oxford: Pergamon Press, 1960.
- [3] A. V. Joura. Electrostatic analogy for static magnetic field. unpublished, 2006.
- [4] G. Tatara and H. Kohno. Theory of current-driven domain wall motion: Spin transfer versus momentum transfer. *Phys. Rev. Lett.*, 92:086601, 2004.
- [5] Eiji Saitoh, Hideki Miyajima, Takehiro Yamaoka, and Gen Tatara. Current-induced resonance and mass determination of a single magnetic domain wall. *Nature*, 432:203, 2004.
- [6] Gen Tatara, Eiji Saitoh, Masahiko Ichimura, and Hiroshi Kohno. Domain wall displacement triggered by an ac current below threshold. *cond-mat/0411292*, 2004.
- [7] Ya. B. Bazaliy. Domain wall motion under the influence of electric current: Phase portrait. unpublished, 2005.
- [8] H. C. Manoharan, C. P. Lutz, and D. M. Eigler. Quantummirages formed by coherent projection of electronic structure. *Nature*, 403:512, 2000.
- [9] G. A. Fiete, J. S. Hersch, E. J. Heller, H. C. Manoharan, C. P. Lutz, and D. M. Eigler. Scattering theory of kondo mirages and observation of single kondo atom phase shift. *Phys. Rev. Lett.*, 86:2392, 2001.
- [10] D. Porras, J. Fernández-Rossier, and C. Tejedor. Microscopic theory for quantum mirages in quantum corrals. *cond-mat/0007445*, 2000.
- [11] M. Weissmann and H. Bonadeo. A simple interpretation of quantum mirages. *cond-mat/0007485*, 2000.
- [12] O. Agam and A. Schiller. Projecting the kondo effect: Theory of the quantum mirage. *cond-mat/0006443*, 2001.
- [13] G. D. Mahan. *Many-particle physics*. New York : Kluwer Academic/Plenum Publishers, 2000.
- [14] M. F. Crommie, C. P. Lutz, and D. M. Eigler. Imaging standing waves in a two-dimensional electron gas. *Nature*, 363, 1993.
- [15] Chris Heilman. The pictorial periodic table. <http://chemlab.pc.maricopa.edu/periodic/Co.html>.
- [16] Mark Winter. Webelements. <http://www.webelements.com/webelements/elements/text/Co/radii.html>.
- [17] N. W. McLachlan. *Theory and application of Mathieu functions*. Oxford : Clarendon, 1951.
- [18] Eric W. Weisstein. Mathieu function. *MathWorld—A Wolfram Web Resource*. <http://mathworld.wolfram.com/MathieuFunction.html>.
- [19] L. D. Landau and E. M. Lifshits. *Quantum mechanics: non-relativistic theory*. Oxford: Pergamon Press, 1977.
- [20] John G. Simmons. Generalized formula for the electric tunnel effect between similar electrodes separated by a thin insulating film. *Journal of Applied Physics*, 34:1793, 1963.